

Contacts to solution-synthesized SnS nanoribbons: Dependence of barrier height on metal work function[†]

Jenifer R. Hajzus,^{*a} Adam J. Biacchi,^b Son T. Le,^b Curt A. Richter,^b Angela R. Hight Walker^b and Lisa M. Porter^a

Abstract

Tin(II) monosulfide (SnS) is a layered, anisotropic material that is of interest as a two-dimensional semiconductor for opto-electronic, thermoelectric, and piezoelectric applications. In this study, the effect of work function on contact behavior was investigated. Ni/Au, Pd/Au, Cr/Au, and Ti/Au contacts were fabricated onto individual, solution-synthesized, p-type SnS nanoribbons. The lower work function metals (Cr and Ti) formed Schottky contacts, whereas the higher work function metals (Ni and Pd) formed ohmic or semi-ohmic contacts. Of the ohmic contacts, Ni was found to have a lower contact resistance ($\sim 10^{-4} \Omega\text{-cm}^2$ or lower) than Pd ($\sim 10^{-3} \Omega\text{-cm}^2$ or lower). Both the calculated Schottky barriers (0.39 and 0.50 eV) for Cr and Ti, respectively, and the ohmic behavior for Ni and Pd agree with behavior predicted by Schottky-Mott theory. The results indicate that high work function metals should be considered to form low resistance contacts to SnS multilayers.

Introduction

The diversity of properties and applications of two-dimensional (2D) materials have vastly expanded since the isolation of graphene¹ as additional layered materials have been investigated. For example, phosphorene, recently exfoliated from black phosphorous (BP),²⁻⁷ is a p-type semiconductor with a thickness-tunable band gap spanning the energy range between graphene and transition metal dichalcogenides (TMDs).⁸ Unlike the hexagonal crystal structure of graphene and most TMDs, phosphorene has an orthorhombic “puckered honeycomb” structure leading to intralayer anisotropy in its optical, electronic, mechanical and thermal properties.⁹ The group-IV monochalcogenides (MX; e.g. M = Sn, Ge; X = S, Se) are a family of layered materials that are isoelectronic with BP. Like BP, their layered structure is buckled, orthorhombic, and anisotropic, but with lower symmetry due to two atomic species. Due to the break in inversion symmetry, IV-VI monolayers are calculated to exhibit significant spin-orbit splitting relevant for spintronics applications¹⁰⁻¹³ and very large piezoelectricity.^{14, 15} They are predicted to be stable in monolayer form, with micromechanical exfoliation being a viable method for producing single-layered material.¹⁶ Additionally, they are expected to be more stable in oxygen-containing environments than phosphorene.^{17, 18} Monolayers of SnSe have been produced by colloidal synthesis¹⁹ and by vapor transport followed by N₂ etching.²⁰

This work focuses on the group-IV monochalcogenide tin sulfide (SnS), which is semiconducting and possesses a thickness-dependent indirect band gap that increases non-monotonically²¹ from approximately 1.1 eV in bulk^{22, 23} to approximately 2 eV in a monolayer.^{11, 16, 21, 23-25} It is natively p-type due to the formation of Sn vacancies, which create shallow acceptors.²⁶ Although a few polytypes of SnS are known to exist, the orthorhombic α -SnS (Fig. 1 a-c) is considered stable at room temperature²⁷; it exists naturally in bulk as the mineral herzenbergite. While monolayer SnS has yet to be isolated, bilayer SnS has been synthesized by liquid-phase exfoliation,^{28, 29} and multilayers have

been synthesized by physical vapor transport,^{30, 31} mechanical exfoliation,³² and solution methods.³³ Interesting properties of SnS monolayers have been proposed such as a high piezoelectric coefficient,¹⁵ high thermoelectric figure of merit (ZT),^{34, 35} ferroelectricity,^{13, 36} ferroelasticity,^{13, 37} and valley pairs selectable by linearly polarized light.^{12, 36} SnS monolayer- and thin film-based van der Waals heterojunctions have also been computationally and experimentally investigated,^{16, 29, 38-41} and electronic properties of SnS nanoribbons have been calculated.⁴² Additionally, SnS multilayers have been experimentally demonstrated in transistors^{31, 32} and photodetectors.^{29, 33}

Over the past two decades, SnS has been studied as an earth abundant, non-toxic absorber layer for thin film solar cells as an alternative to copper indium gallium selenide (CIGS) and CdTe.^{43, 44} Bulk SnS has a high absorption coefficient of around 10^4 cm^{-1} and a band gap that is close to ideal for photoconversion according to the Shockley–Queisser limit, with calculated efficiencies reaching 24 %.⁴⁵ However, the highest experimental efficiency reported for SnS-based solar cells is 4.36 %.⁴⁶ Resistive losses at the back contact are considered an important loss mechanism in these cells. Highly resistive contacts can also obscure the measurement of intrinsic properties of emerging materials.^{47, 48} High contact resistances can be due to a Schottky barrier height, Φ_B , at the metal-semiconductor interface. Schottky-Mott theory states that for a p-type semiconductor, Φ_B is equal to the sum of the semiconductor band gap (E_g) and electron affinity (χ) minus the work function of the metal (Φ_M). In practice, however, many semiconductors, such as multilayer MoS₂,⁴⁸⁻⁵⁰ exhibit a weak dependence of barrier height on metal work function due to Fermi level pinning.

In this work, the electrical behavior of four different metal contacts to individual SnS nanoribbons was investigated. Metals with a range of work functions were selected:⁵¹ Ti ($\Phi_M = 4.33 \text{ eV}$), Cr ($\Phi_M = 4.50 \text{ eV}$), Ni ($\Phi_M = 5.15 \text{ eV}$),⁵² and Pd ($\Phi_M = 5.22 \text{ eV}$). Current-voltage measurements of device structures fabricated using e-beam lithography were used to establish whether the contacts were ohmic or rectifying. Contact resistances and Schottky barrier heights were calculated from the measurements. From the results, a model for band alignments between the metals and SnS is proposed; this model agrees with that predicted based on the Schottky-Mott model and reported properties in the published literature. To the best of the authors' knowledge, this is the first reported analysis of contact performance on devices fabricated from individual colloidal semiconductor nanocrystals.

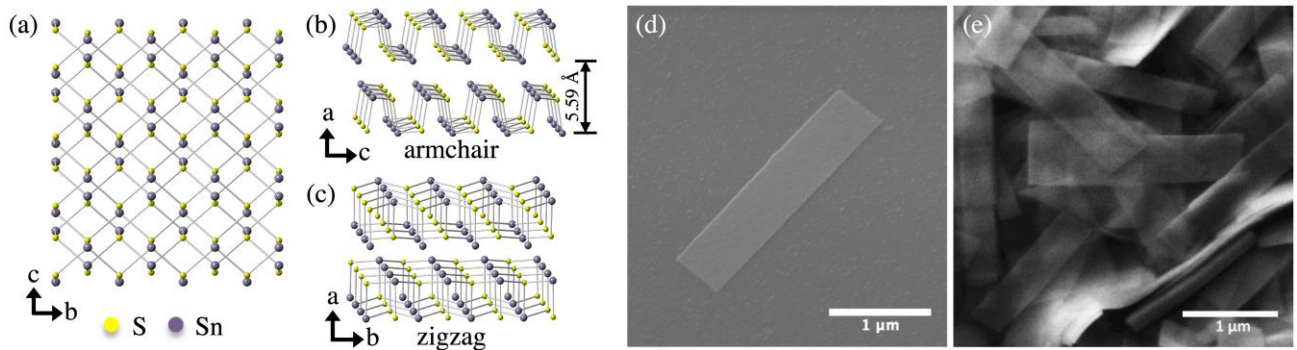


Fig 1. Orthorhombic *Pnma* crystal structure of α -SnS viewing from the (a) (100) plane, and slightly tilted from the (b) (010), and (c) (001) planes. Lattice constants are $a = 1.1180 \text{ nm}$, $b = 0.3982 \text{ nm}$, and $c = 0.4329 \text{ nm}$.⁵³ SEM images of (d) a solution-synthesized nanoribbon on a SiO₂/Si substrate and (e) a high concentration of nanoribbons.

Experimental

Device Fabrication

Colloidal SnS nanoribbons were synthesized in solution using a procedure described elsewhere (see supporting information for details).⁵⁴ The resulting semiconductor nanocrystals are several μm in length, but only 20 nm or less in thickness (Fig. 1 d,e and supporting information, Fig. S1). Our previous studies indicate that these nanoribbons are phase-pure orthorhombic SnS, with p-type conductivity and a hole concentration estimated to be on the order of 10^{16} cm^{-3} .⁵⁴ Diluted SnS nanoribbon dispersions in toluene were spin coated at 314 rad/s (3,000 rpm) for 30 seconds onto a $\text{SiO}_2/\text{p}++\text{Si}$ substrate with Ti/Au fiduciary marks and a Ni/Au ohmic back contact (Fig. 2 a). The thermal oxide thickness was 100 nm. Following deposition, excess toluene was evaporated in an oven at 80 °C for 1 minute. Samples were then placed in a 2" quartz tube furnace and annealed at 375 °C for 15 minutes in forming gas (5 % H_2 /95 % Ar, flow rate 800 sccm). Previous spectroscopic analysis has indicated that annealing under these reducing conditions fully removes residual organics from the surface.^{54, 55}

Contacts were patterned to individual nanoribbons using electron-beam lithography (Zeiss NVision 40 FESEM with Raith Elphy Quantum) (Fig. 2 b and supporting information, Fig. S2). Three different contact configurations were used: (1) two large contacts spaced 1 μm apart; (2) three contacts of equivalent length with spacings of 500 nm and 1 μm ; and (3) four contacts of equivalent length with spacings of 250 nm, 500 nm, and 1 μm (Fig. 2 c). Contact lengths were designed to be either 250 nm or 500 nm.

Prior to metal deposition, samples were dipped in 1% hydrofluoric acid (HF) for 30 s, dipped in deionized water for 30 s, and then blown dry with N_2 . Samples were immediately (within 5 min to 10 min) loaded into an e-beam evaporation system (Thermionics) with a base pressure in the 10^{-7} Pa (10^{-9} Torr) range. All metals were evaporated at a rate of 0.1 nm/s, as monitored by a quartz crystal microbalance (QCM). For each contact scheme, 40 nm of the selected metal was deposited, followed by 40 nm of Au. The purities of the commercial metal sources were: 99.995 % Ni, 99.95 % Pd, 99.996 % Cr, 99.995 % Ti and 99.999 % Au. Following evaporation, liftoff was performed in acetone.

Characterization

Electrical measurements were performed in the dark with a Signatone S-1060H-4QR probe station connected to an Agilent HP 4155C semiconductor parameter analyzer with voltage measurement input resistance $> 10^{13} \Omega$. Scanning electron microscope (SEM) micrographs were acquired with either a Phillips XL30 FESEM or Zeiss InVision 40 FESEM and were used to determine contact dimensions and channel lengths (supporting information, Fig. S3). A minimum of 15 pairs of contacts were analyzed for each deposited metal. Diffuse reflectance spectra were collected on dropcast films of SnS nanoribbons with a Perkin-Elmer Lambda 950 spectrophotometer equipped with a 150 mm integrating sphere.

Results and Discussion

Current-voltage sweeps were performed between adjacent contact pairs, and results are presented in Fig. 2 d,e. The total resistance between contacts decreases from Ti/Au, Cr/Au, Pd/Au, to Ni/Au. Additionally, Schottky behavior was observed for the contact metals with low work functions (Cr and Ti), whereas ohmic or semi-ohmic behavior was exhibited for the contact metals with high work

functions (Ni and Pd). These results were consistent for the 15 – 28 pairs of contacts that were analyzed for each metal. To quantify the electrical behavior of the contacts, measurements were conducted to calculate Schottky barrier heights and specific contact resistances of the Schottky and ohmic contacts, respectively.

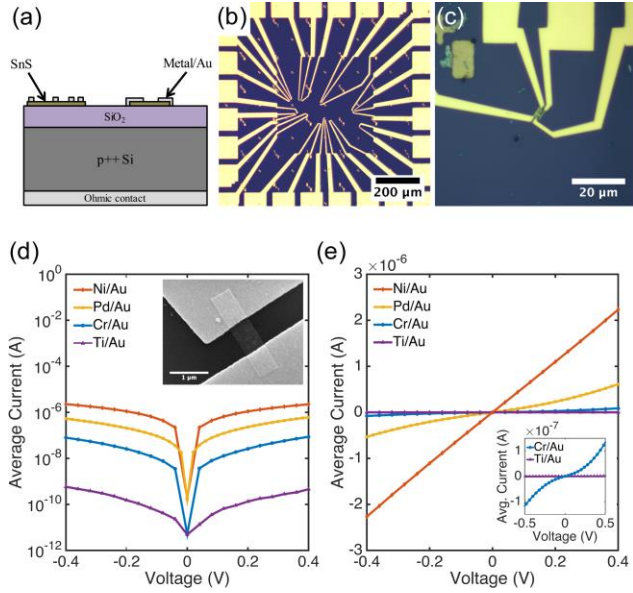


Fig. 2 (a) Cross sectional schematic of device structure. Two nanoribbons with different contact configurations are shown. (b) Optical microscope image of a sample with many contact test structures patterned in one area and (c) a higher magnification image of a nanoribbon with four contacts. Average I-V sweeps for each contact metallization with 1 μm channel spacing on a (d) log and (e) linear scale, showing ohmic and semi-ohmic behavior for Pd/Au and Ni/Au contacts, and Schottky behavior for Cr/Au and Ti/Au contacts. Inset in (d) is an SEM image of a two contact Ni/Au device.

Schottky barrier height I-V measurement

The Cr and Ti Schottky contact pairs consist of two back-to-back Schottky diodes in series, separated by a SnS channel length. Different methods have been developed to analyze the room temperature I-V behavior of such a configuration.⁵⁶⁻⁵⁸ Here, a method similar to those of Chiquito *et al.*⁵⁹ and Nouchi *et al.*⁶⁰ is used. The total current through the device is

$$I = \frac{2I_{01}I_{02} \sinh\left(\frac{qV}{2kT}\right)}{I_{01} \exp\left(-\frac{qV}{2kT}\right) + I_{02} \exp\left(\frac{qV}{2kT}\right)}, \quad (1)$$

where V is the applied voltage, q is the elementary charge, k is Boltzmann's constant, and T is temperature (see supporting information for derivation). $I_{01,02}$ is the saturation current given by

$$I_{01} = S_1 A^{**} T^2 \exp\left(\frac{q\phi_1}{kT}\right) \quad (2a)$$

$$I_{02} = S_2 A^{**} T^2 \exp\left(\frac{q\phi_2}{kT}\right), \quad (2b)$$

where A^{**} is the effective Richardson constant, $\Phi_{1,2}$ are the effective Schottky barrier heights, and $S_{1,2}$ are the contact areas; the subscripts refer to diodes 1 and 2, respectively.

Ideality factors, $n_{1,2}$, can be introduced to account for a voltage dependence of the Schottky barrier height.⁶¹ The voltage dependence of the barrier height is a consequence of image force lowering, and in some cases an interfacial layer and interface states.^{61, 62} The ideality factor can also increase due to tunneling through the barrier or carrier recombination in the depletion region. A characteristic energy, E_{00} , was calculated to determine the conduction mechanism at the interface.⁶³ When E_{00} is much smaller than the thermal energy (kT), thermionic emission is expected.⁶⁴ Room temperature tunneling is not expected in forward bias at these doping concentrations, as $E_{00} \approx 0.7$ meV (calculated using a dielectric constant of 32.8^{14, 65, 66} and hole effective mass of $0.23m_0$ ^{21, 23, 67}). However, tunneling and image force lowering may have a greater impact in reverse bias.^{61, 63} Additionally, there have been reports of larger tunneling contributions for very thin nanostructures.^{48, 68} Taking into account the ideality factor, the modified barrier height is written as^{59, 61}

$$\Phi_{1,2} = \Phi_{01,02} + V \left(\frac{1}{n_{1,2}} - 1 \right), \quad (3)$$

where $\Phi_{01,02}$ are the true Schottky barrier heights for diodes 1 and 2, respectively.

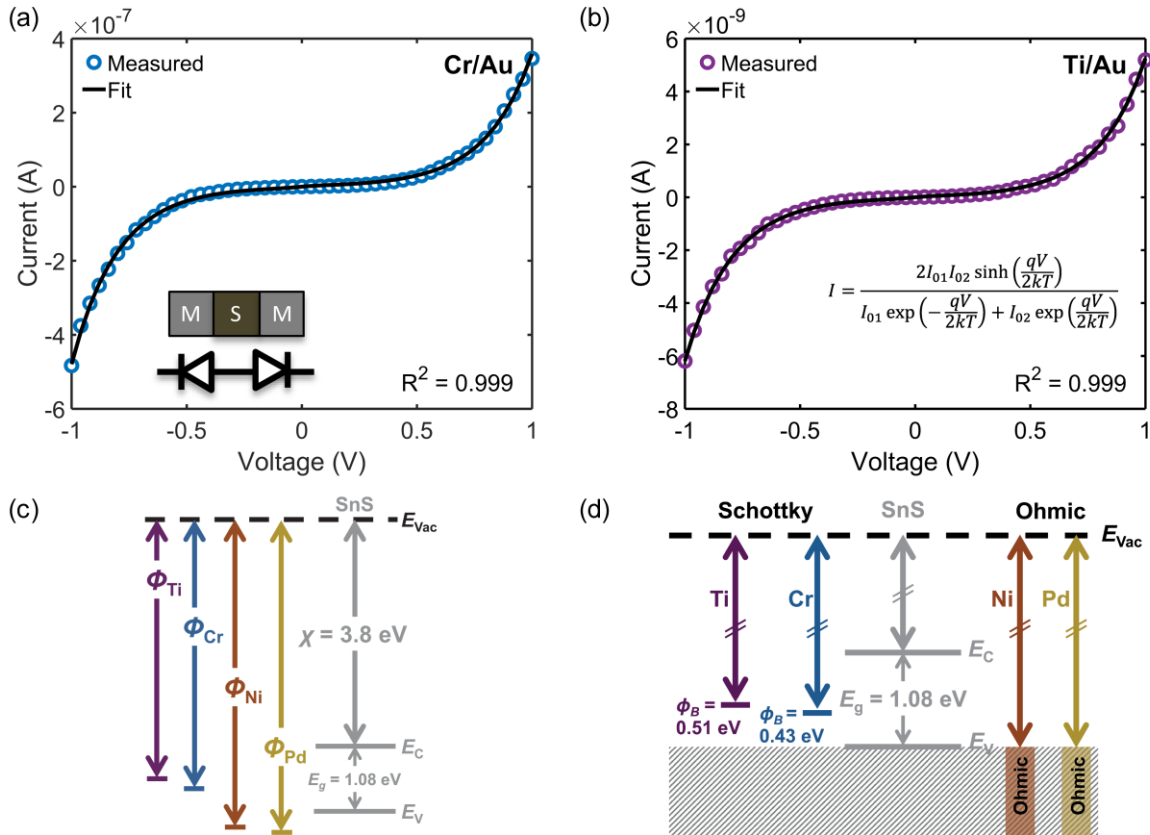


Fig. 3. Example fits of I-V sweeps to the back-to-back Schottky diode equation for (a) Cr/Au contacts on SnS and (b) Ti/Au contacts on SnS. I-V sweeps were measured between adjacent contacts. (c) Schottky-Mott band alignment of metals and SnS. χ is the electron affinity of SnS, E_g is the band gap, E_{vac} is the vacuum level, E_c is the conduction band minimum, and E_v is the valence band maximum. (d) Experimental band alignment.

The I-V curves were fit to Equations 1-3 using a nonlinear least squares method. The Richardson's constant used was 27.6 A/($\text{cm}^2\text{-K}^2$), which was calculated with literature values for the

bulk SnS hole effective mass in the zigzag direction.^{21, 23, 67} It was found that the value used for Richardson's constant did not greatly impact the extracted fit parameters.

Example fits for Cr/Au and Ti/Au back-to-back Schottky contacts are shown in Fig. 3 a,b. As indicated by the fit parameters listed in Table 1, the calculated average Schottky barrier heights at the interface with SnS nanoribbons were 0.39 eV and 0.50 eV for Cr/Au and Ti/Au, respectively. These values are in close agreement with the values ($\Phi_{B,Cr} = 0.38$ eV and $\Phi_{B,Ti} = 0.55$ eV) predicted by the Schottky-Mott metal-semiconductor band alignment model (Fig. 3 c). The electron affinity listed is a reported value for the (100) surface of bulk SnS.⁶⁹ The band gap of bulk SnS has been reported to be 1.08 eV⁷⁰ and confirmed experimentally using diffuse reflectance spectroscopy (supporting information, Fig. S4).⁷¹

Table I. Average fit parameters for Cr/Au and Ti/Au Schottky contacts. Φ_B is the average of Φ_{01} and Φ_{02} , and n the average of n_1 and n_2 .

Metal	Φ_B (eV)	n	R^2	No. Devices
Cr/Au	0.39 ± 0.05	1.12 ± 0.02	0.996 ± 0.002	20
Ti/Au	0.50 ± 0.06	1.13 ± 0.07	0.996 ± 0.003	15

The experimentally determined alignment is depicted in Fig. 3 d; the alignments of the ohmic contacts are assumed to be near or below the valence band maximum. The results indicate a lack of Fermi-level pinning and agree with a recent report of ohmic Ni contacts on 50 nm to 100 nm thick multilayer 2D SnS.³² Additionally, an older study reports Ag Schottky contacts to the (100) plane of bulk SnS with a barrier height of 0.649 eV.⁷² Although the work function of metals can vary depending on orientation and processing, this barrier height value is close to the 0.62 eV value predicted here for polycrystalline Ag ($\Phi_M = 4.26$ eV).⁷³

While ideality factors are low, they are higher than those expected for only image force lowering at this moderate doping concentration. This suggests an additional contribution to the ideality factor, such as from tunneling or an interfacial layer. SnS is known to form a thin native oxide at its surface,⁷⁴ which we have observed previously using X-ray photoelectron spectroscopy.⁵⁵ The oxide can be removed under reducing conditions but regrows upon exposure to ambient air. While samples were dipped in HF prior to metal deposition, further study is needed to determine the effect this may have on the oxide layer. There have been reports of oxide layers impacting Schottky barrier heights to MoS₂.⁷⁵⁻⁷⁸

Specific contact resistance measurement

The specific contact resistance was measured for the ohmic Ni/Au and semi-ohmic Pd/Au contacts. For bulk semiconductors, the specific contact resistance can be measured by a transfer length method (TLM), involving four or more contacts with varying spacings. Due to the confined lengths of the nanoribbons, some were too small for a four contact TLM pattern. For those nanostructures, three contacts were patterned, and a contact end resistance (CER)⁷⁹ measurement combined with a three-probe contact front resistance measurement were used.⁶⁴

The current in a metal-semiconductor contact encounters two competing resistances- the semiconductor sheet resistance, R_{sh} , and an interfacial resistance, which is experimentally quantified by the specific contact resistance, ρ_c . The interface is described by a transmission line model represented in Fig. 4 a^{79, 80} The voltage distribution under the contact as a function of distance is given by⁷⁹,

$$V(x) = \frac{i_1 \sqrt{R_{sh} \rho_c} \cosh\left(\frac{L-x}{L_T}\right)}{Z \sinh\left(\frac{L}{L_T}\right)}, \quad (4)$$

where i_1 is the current flowing into the contact, L is the length of the contact, Z is the width of the contact, x is the distance along the contact ($x = 0$ is the front of the contact and $x = L$ is the end of the contact), ρ_c is the specific contact resistance, and L_T is the transfer length. The transfer length is given by ^{64, 79}

$$L_T = \sqrt{\rho_c / R_{sh}}. \quad (5)$$

For long contacts ($L > 3L_T$), Eq. 4 can be approximated as an exponential function and L_T is the distance under the contact in which $1 - (1/e)$ of the current has entered the metal.

Contact end resistance

The measurement configuration for the CER method is depicted in Fig. 4 b. Here, three contacts with equal L and unequal spacings between contacts, d , were fabricated on single nanoribbons (Fig. 4 c). Current, I_{12} , was applied between contacts 1 and 2, and voltage, V_{23} , was measured between contacts 2 and 3 (Fig. 4 d). The current flowing between contacts 2 and 3 is negligible when a high impedance voltage measurement unit is used. Therefore, this configuration provides a voltage sampling at the end of the contact (i.e., at $x = L$). From Eq. 4 and Eq. 5, the contact end resistance, R_{ce} , is given as

$$R_{ce} = \frac{V_{23}}{I_{12}} = \frac{\rho_c}{L_T Z} \frac{1}{\sinh\left(\frac{L}{L_T}\right)}. \quad (6)$$

Alternatively, when current, I_{12} , is measured between contacts 1 and 2, and voltage, V_{12} is applied between contacts 1 and 2, the voltage is sampled at the front of the contact (i.e., at $x = 0$). From Eq. 4 and 5, the contact front resistance, R_{cf} , can be written as

$$R_{cf} = \frac{\rho_c}{L_T Z} \coth\left(\frac{L}{L_T}\right). \quad (7)$$

R_{cf} was determined as shown in Fig. 4 e, where the total resistance between contacts 1 and 2 (R_{12}), and between 2 and 3 (R_{23}) were measured. The total resistance is⁶⁴

$$R_{12,23} = \frac{R_{sh} d_{12,23}}{Z} + 2R_{cf}, \quad (8)$$

where $d_{12,23}$ are the spacings between contacts 1 and 2 or 2 and 3, respectively. Assuming the contact resistances for all three contacts are identical, R_{cf} can be solved for as ⁷⁹

$$R_{cf} = \frac{R_{23} d_{12} - R_{12} d_{23}}{2(d_{12} - d_{23})}. \quad (9)$$

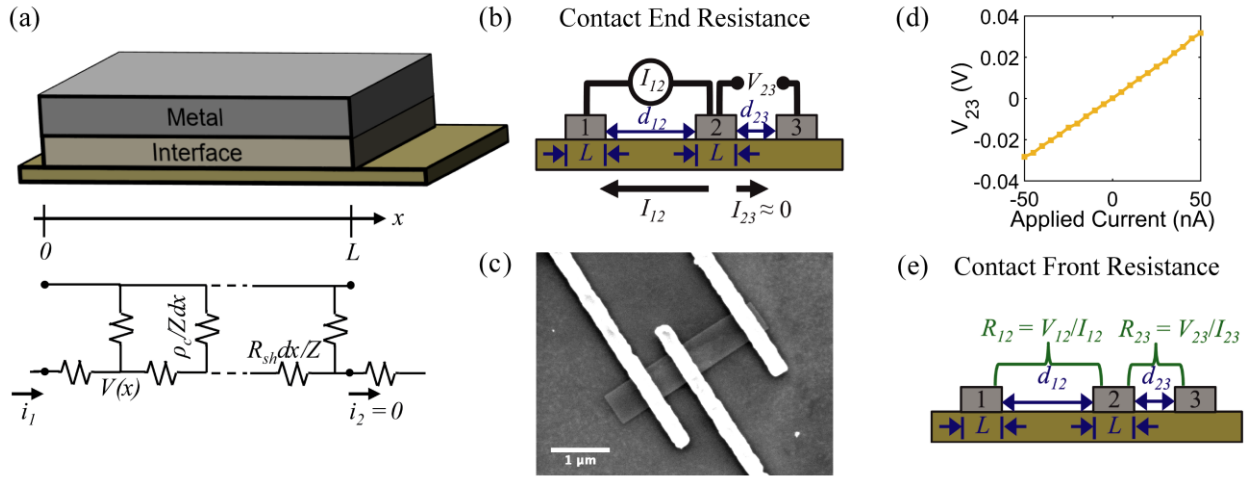


Fig. 4. (a) Transmission line model for metal-semiconductor contact. (b) Schematic of contact end resistance measurement. (c) SEM image of a CER structure for Ni/Au contacts on a SnS nanoribbon. (d) Example measurement of V_{23} for contact end resistance measurement of a set of Pd/Au contacts. (e) Schematic of contact front resistance measurement.

The transfer length was determined by taking the ratio of the contact end and front resistances,

$$\frac{R_{ce}}{R_{cf}} = \frac{1}{\cosh\left(\frac{L}{L_T}\right)}, \quad (10)$$

and the calculated L_T value was subsequently inserted into Eq. 6 or 7 to solve for ρ_c . R_{sh} was then calculated from Eq. 5.

The results of these measurements are displayed in Table 2. It can be seen that the calculated specific contact resistances of the Pd/Au contacts are higher than those of Ni/Au. The extracted transfer lengths were in most cases approximately equal to the length of the contacts or smaller, and in only a few cases, slightly longer. It was found that the calculated specific contact resistances of devices with transfer lengths longer than the contact were similar to those with shorter transfer lengths. The long transfer lengths will be discussed in terms of the transmission line model in the next section.

The measured sheet resistance is lower for Ni/Au contacts than Pd/Au contacts. In this method, the extracted sheet resistance is the sheet resistance of the nanoribbon underneath the contact region. A few factors could alter the nanoribbon sheet resistance under the contact, such as a reaction at the interface (Pd and Ni are both thermodynamically predicted to react with SnS^{81, 82}), or a depletion width on the order of the thickness (the depletion width is on the order of a few hundred nanometers at this doping density). The variation in sheet resistance and contact resistance values may be a result of different amounts of reactions at the interface between devices.

Table 2. Specific contact resistances and related parameters, calculated using the contact end resistance method.

Metal	R_{cf} (Ω)	R_{ce} (Ω)	L (nm)	L_T (nm)	R_{sh} (Ω/\square)	ρ_c ($\Omega \cdot \text{cm}^2$)
Ni/Au	$4.3 (\pm 3.2) \times 10^4$	$2.8 (\pm 2.2) \times 10^4$	$3.7 (\pm 0.7) \times 10^2$	$3.5 (\pm 0.4) \times 10^2$	$6.1 (\pm 4.9) \times 10^4$	$5.4 (\pm 3.9) \times 10^{-5}$
Pd/Au	$2.5 (\pm 1.3) \times 10^6$	$7.3 (\pm 1.1) \times 10^5$	$2.8 (\pm 0.2) \times 10^2$	$2.2 (\pm 1.2) \times 10^2$	$7.9 (\pm 7.1) \times 10^6$	$1.3 (\pm 0.3) \times 10^{-3}$

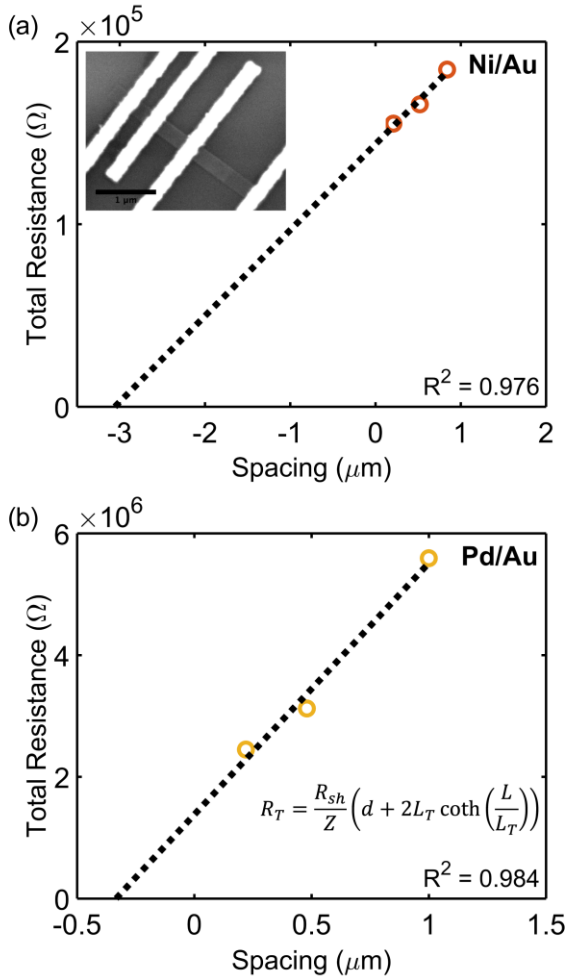


Fig. 5. Transfer length method (TLM) plots for extracting sheet resistance, specific contact resistance, and transfer lengths of contacts on an individual SnS nanoribbon for (a) Ni/Au contacts and (b) Pd/Au contacts. Inset in (a) is an SEM image of a representative TLM device.

Transfer length method (TLM)

For longer nanoribbons, a TLM design was patterned, consisting of four contacts on a single nanoribbon. The four contacts of equal length were separated by varying channel spacings, d . The total resistance, R_T , was measured between each set of adjacent contacts and is equal to the sum of the resistance contribution from the semiconductor, $(R_{sh}d)/Z$, and the two contact resistances, $2R_{cf}$. When R_T is plotted as a function of d , the y -intercept corresponds to the resistance contribution from the two contacts only and is equal to $2R_{cf}$. R_{sh} can be determined from the slope, and L_T can be determined by extrapolating the x -intercept.^{64,83} Typically, this method makes use of the approximation that when $L \geq 3L_T$, the $\coth(L/L_T)$ term in Eq. 7 is approximately equal to 1, and therefore the x -intercept is equal to $-2L_T$. However, Table 2 indicates that $L \geq 3L_T$ is not valid for the geometries here, so this approximation cannot be used. Therefore, the full Eq. 7 was used, yielding a total resistance:

$$R_T = \frac{R_{sh}}{Z} \left(d + 2L_T \coth\left(\frac{L}{L_T}\right) \right). \quad (11)$$

In this case, the x -intercept is equal to $-2L_T \coth(L/L_T)$, and the y -intercept and slope remain equal to $2R_{cf}$ and R_{sh}/Z , respectively. A similar expression was derived for contacts to semiconductor nanowires with short contact lengths.⁸⁴

The specific contact resistance can also be written in terms of the contact resistance multiplied by the area of the contact. For long contacts ($L > 3L_T$), the transfer length is used for the length, and, from Eq. 7, $R_{cf} \approx \rho_c/(L_T Z)$.⁶⁴ For very short contacts, $R_{cf} \approx \rho_c/(L Z)$.⁶⁴ For the intermediate contact lengths here, neither approximation can be used, but an effective length can be defined, such that

$$L_{eff} = \frac{L_T}{\coth\left(\frac{L}{L_T}\right)}. \quad (12)$$

Then, $R_{cf} = \rho_c/(L_{eff} Z)$. Equation 4 is derived for a terminal contact, in which all current is collected between $x=0$ and $x=L$ such that i_2 in Fig. 4 a is equal to zero.⁷⁹ When the contact length becomes less than $3L_T$, R_{cf} begins to increase. $i_1 R_{cf}$ multiplied by L_{eff} is equal to the integral of the voltage along the entire contact, such that $\frac{1}{i_1} \int_0^L V(x) dx = R_{cf} \cdot L_{eff}$. The specific contact resistance can therefore be calculated by multiplying the measured R_{cf} by the contact width and effective length, or by solving for ρ_c in Eq. 5 ($\rho_c = L_T^2 \cdot R_{sh}$). This approach assumes all current is collected within the length of the contact and does not take into account spreading resistance beyond the length of the contact.

Table 3. Specific contact resistance parameters extracted by transfer length method (TLM) for Ni/Au and Pd/Au contacts.

Metal	R^2	R_{cf} (Ω)	L (nm)	L_T (nm)	L_{eff} (nm)	R_{sh} (Ω/\square)	ρ_c ($\Omega \cdot \text{cm}^2$)
Ni/Au	0.976	$7.2 (\pm 0.2) \times 10^4$	2.9×10^2	$6.4 (\pm 0.5) \times 10^2$	$2.7 (\pm 0.3) \times 10^2$	$2.7 (\pm 0.4) \times 10^4$	$1.1 (\pm 0.3) \times 10^{-4}$
Pd/Au	0.984	$6.9 (\pm 1.7) \times 10^5$	3.0×10^2	$1.6 (\pm 0.5) \times 10^2$	$1.5 (\pm 0.5) \times 10^2$	$2.3 (\pm 0.3) \times 10^6$	$5.9 (\pm 3.6) \times 10^{-4}$

Plots of R_T vs d are displayed in Fig. 5, and Table 3 lists extracted parameters. Similar to the results extracted by the CER method, it is observed that the specific contact resistance of Ni is lower than that of Pd, and the extracted sheet resistance for Ni is lower than that of Pd. In this case, the transfer length for the Ni/Au contact is larger than the length of the contact, and the transfer length of Pd/Au was greater than $L/3$. As previously discussed, the specific contact resistances can be calculated using $R_{cf} = \rho_c/(L_{eff} Z)$, which are equivalent to the ρ_c calculated by Eq. 5 and Eq. 11. Since R_{cf} will increase with decreasing contact length when the contact length is less than $3L_T$, this indicates that in devices, a contact length longer than those used here would be ideal to further reduce R_{cf} .

The TLM assumes the sheet resistance under the contact is equal to the nanoribbon sheet resistance in the channel. In reality, this may not be the case due to factors such as reactions at the interface or the depletion width being on the order of the thickness of the semiconductor.⁸⁵ An additional measurement of R_{ce} can take into account a change in underlying R_{sh} .^{85, 86} The contact end resistance measurement was performed on the Ni/Au TLM structure, and, in conjunction with R_{cf} determined by the TLM measurement, specific contact resistance parameters were extracted. The sheet resistance determined by incorporating this additional measurement was $3.3 \times 10^3 \Omega/\square$, which is lower than that measured by the TLM method alone ($2.7 \times 10^4 \Omega/\square$). This suggests the sheet resistance

in the SnS region underneath the Ni/Au contact is lower than the sheet resistance of the pristine SnS channel and therefore may indicate a reaction occurred at the Ni/SnS interface. Further studies would be required to determine the exact nature of the Ni/SnS interface. Possible reaction products of bulk SnS and Ni calculated from FactSage®⁸¹ include Ni₃Sn₂ and Ni₃S₂. It is interesting to note that the work function of Ni₃S₂ has been reported to be ~5 eV,^{87, 88} which is similar to that of unreacted Ni; whereas the work function of Ni₃Sn₂ may be as low as 4.55 eV.⁸⁹ Regardless of whether a reaction has occurred at this interface, Ni contacts to SnS nanoribbons appear to behave as predicted by the Schottky-Mott model for a high work function metal.

Conclusion

In this work, Ni, Pd, Cr, and Ti contact test structures were fabricated onto individual, solution-synthesized, p-type SnS nanoribbons. We conducted what we believe to be the first reported analysis of contact performance in devices fabricated from colloidal nanocrystals. The high work function metals (Ni and Pd) formed ohmic or semi-ohmic contacts to SnS nanoribbons, while the lower work function metals (Cr and Ti) formed Schottky contacts. The Schottky barrier heights calculated for Cr and Ti agree well with the band alignment predicted by Schottky-Mott theory, whereas the ohmic behavior of Ni and Pd also agree with the expectations from this model. Of the two ohmic metals, a lower specific contact resistance (on the order of 10⁻⁴ Ω-cm² or lower) was consistently calculated for Ni. The results of this study indicate a lack of Fermi level pinning in metal-SnS nanoribbon structures and can inform the selection of contact metals in the design of future SnS-based devices.

Conflicts of Interest

The authors declare no competing financial interest. Certain commercial equipment or materials are identified in this paper to adequately specify the experimental procedures. In no case does the identification imply recommendation or endorsement by NIST, nor does it imply that the materials or equipment identified are necessarily the best available for the purpose.

Acknowledgements

The authors acknowledge the support of the Bertucci Graduate Fellowship at Carnegie Mellon University (J.R.H.), the NIST Director's Fellow Postdoctoral Research Associateship program (A.J.B.) and NIST-STRS for funding. The authors also acknowledge use of the Materials Characterization Facility at Carnegie Mellon University supported by grant MCF-677785. Research was performed in part at the NIST Center for Nanoscale Science and Technology with support from a CNST-UMD Collaboration Travel Grant. We thank Kerry Siebein for her assistance with characterization and fabrication and Yi Luo for valuable discussions. A.J.B. gratefully acknowledges emeritus NIST fellow Herbert Bennett.

References

1. K. S. Novoselov, A. K. Geim, S. V. Morozov, D. Jiang, Y. Zhang, S. V. Dubonos, I. V. Grigorieva and A. A. Firsov, *Science*, 2004, **306**, 666-669.
2. L. K. Li, Y. J. Yu, G. J. Ye, Q. Q. Ge, X. D. Ou, H. Wu, D. L. Feng, X. H. Chen and Y. B. Zhang, *Nat. Nanotechnol.*, 2014, **9**, 372-377.
3. A. Castellanos-Gomez, L. Vicarelli, E. Prada, J. O. Island, K. L. Narasimha-Acharya, S. I. Blanter, D. J. Groenendijk, M. Buscema, G. A. Steele, J. V. Alvarez, H. W. Zandbergen, J. J. Palacios and H. S. J. van der Zant, *2D Mater.*, 2014, **1**, 025001.
4. S. P. Koenig, R. A. Doganov, H. Schmidt, A. H. C. Neto and B. Ozyilmaz, *Appl. Phys. Lett.*, 2014, **104**, 103106.
5. F. N. Xia, H. Wang and Y. C. Jia, *Nat. Commun.*, 2014, **5**, 4458.
6. J. S. Qiao, X. H. Kong, Z. X. Hu, F. Yang and W. Ji, *Nat. Commun.*, 2014, **5**, 4475.
7. H. Liu, A. T. Neal, Z. Zhu, Z. Luo, X. F. Xu, D. Tomanek and P. D. D. Ye, *ACS Nano*, 2014, **8**, 4033-4041.
8. A. H. Woomer, T. W. Farnsworth, J. Hu, R. A. Wells, C. L. Donley and S. C. Warren, *ACS Nano*, 2015, **9**, 8869-8884.
9. X. Ling, H. Wang, S. X. Huang, F. N. Xia and M. S. Dresselhaus, *Proc. Natl. Acad. Sci. U. S. A.*, 2015, **112**, 4523-4530.
10. K. S. Novoselov, A. Mishchenko, A. Carvalho and A. H. C. Neto, *Science*, 2016, **353**, aac9439.
11. L. C. Gomes and A. Carvalho, *Phys. Rev. B*, 2015, **92**, 085406.
12. A. S. Rodin, L. C. Gomes, A. Carvalho and A. H. C. Neto, *Phys. Rev. B*, 2016, **93**, 045431.
13. M. H. Wu and X. C. Zeng, *Nano Lett.*, 2016, **16**, 3236-3241.
14. L. C. Gomes, A. Carvalho and A. H. C. Neto, *Phys. Rev. B*, 2015, **92**, 214103.
15. R. Fei, W. Li, J. Li and L. Yang, *Appl. Phys. Lett.*, 2015, **107**, 173104.
16. A. K. Singh and R. G. Hennig, *Appl. Phys. Lett.*, 2014, **105**, 042103.
17. L. C. Gomes, A. Carvalho and A. H. C. Neto, *Phys. Rev. B*, 2016, **94**, 054103.
18. Y. Guo, S. Zhou, Y. Z. Bai and J. J. Zhao, *ACS Appl. Mater. Interfaces*, 2017, **9**, 12013-12020.
19. L. Li, Z. Chen, Y. Hu, X. W. Wang, T. Zhang, W. Chen and Q. B. Wang, *J. Am. Chem. Soc.*, 2013, **135**, 1213-1216.
20. J. Z. Jiang, C. P. Y. Wong, J. Zou, S. S. Li, Q. X. Wang, J. Y. Chen, D. Y. Qi, H. Y. Wang, G. Eda, D. H. C. Chua, Y. M. Shi, W. J. Zhang and A. T. S. Wee, *2D Mater.*, 2017, **4**, 021026.
21. C. Xin, J. X. Zheng, Y. T. Su, S. K. Li, B. K. Zhang, Y. C. Feng and F. Pan, *J. Phys. Chem. C*, 2016, **120**, 22663-22669.
22. G. Valiukonis, D. A. Guseinova, G. Krivaite and A. Sileika, *Phys. Status Solidi B*, 1986, **135**, 299-307.
23. G. A. Tritsarlis, B. D. Malone and E. Kaxiras, *J. Appl. Phys.*, 2013, **113**, 233507.
24. L. Huang, F. G. Wu and J. B. Li, *J. Chem. Phys.*, 2016, **144**, 114708.
25. C. Chowdhury, S. Karmakar and A. Datta, *J. Phys. Chem. C*, 2017, **121**, 7615-7624.
26. J. Vidal, S. Lany, M. d'Avezac, A. Zunger, A. Zakutayev, J. Francis and J. Tate, *Appl. Phys. Lett.*, 2012, **100**, 032104.
27. L. A. Burton and A. Walsh, *J. Phys. Chem. C*, 2012, **116**, 24262-24267.
28. J. R. Brent, D. J. Lewis, T. Lorenz, E. A. Lewis, N. Savjani, S. J. Haigh, G. Seifert, B. Derby and P. O'Brien, *J. Am. Chem. Soc.*, 2015, **137**, 12689-12696.
29. Z. Y. Jia, S. L. Li, J. Y. Xiang, F. S. Wen, X. Bao, S. H. Feng, R. L. Yang and Z. Y. Liu, *Nanoscale*, 2017, **9**, 1916-1924.

30. J. Xia, X. Z. Li, X. Huang, N. N. Mao, D. D. Zhu, L. Wang, H. Xu and X. M. Meng, *Nanoscale*, 2016, **8**, 2063-2070.
31. Z. Tian, C. L. Guo, M. X. Zhao, R. R. Li and J. M. Xue, *ACS Nano*, 2017, **11**, 2219-2226.
32. S. Sucharitakul, U. R. Kumar, R. Sankar, F. C. Chou, Y. T. Chen, C. H. Wang, C. He, R. He and X. P. A. Gao, *Nanoscale*, 2016, **8**, 19050-19057.
33. Z. Deng, D. Cao, J. He, S. Lin, S. M. Lindsay and Y. Liu, *ACS Nano*, 2012, **6**, 6197-6207.
34. L. M. Sandonas, D. Teich, R. Gutierrez, T. Lorenz, A. Pecchia, G. Seifert and G. Cuniberti, *J. Phys. Chem. C*, 2016, **120**, 18841-18849.
35. S. D. Guo and Y. H. Wang, *J. Appl. Phys.*, 2017, **121**, 034302.
36. P. Z. Hanakata, A. Carvalho, D. K. Campbell and H. S. Park, *Phys. Rev. B*, 2016, **94**, 035304.
37. H. Wang and X. F. Qian, *2D Mater.*, 2017, **4**, 015042.
38. W. Q. Xiong, C. X. Xia, X. Zhao, T. X. Wang and Y. Jia, *Carbon*, 2016, **109**, 737-746.
39. K. Cheng, Y. Guo, N. N. Han, Y. Su, J. F. Zhang and J. J. Zhao, *J. Mater. Chem. C*, 2017, **5**, 3788-3795.
40. R. Browning, P. Plachinda, P. Padigi, R. Solanki and S. Rouvimov, *Nanoscale*, 2016, **8**, 2143-2148.
41. W. Wang, K. K. Leung, W. K. Fong, S. F. Wang, Y. Y. Hui, S. P. Lau, Z. Chen, L. J. Shi, C. B. Cao and C. Surya, *J. Appl. Phys.*, 2012, **111**, 093520.
42. M. J. Zhang, Y. P. An, Y. Q. Sun, D. P. Wu, X. N. Chen, T. X. Wang, G. L. Xu and K. Wang, *Phys. Chem. Chem. Phys.*, 2017, **19**, 17210-17215.
43. J. A. Andrade-Arvizu, M. Courel-Piedrahita and O. Vigil-Galan, *J. Mater. Sci.: Mater. Electron.*, 2015, **26**, 4541-4556.
44. L. A. Burton, D. Colombara, R. D. Abellon, F. C. Grozema, L. M. Peter, T. J. Savenije, G. Dennler and A. Walsh, *Chem. Mater.*, 2013, **25**, 4908-4916.
45. R. E. Banai, M. W. Horn and J. R. S. Brownson, *Sol. Energy Mater. Sol. Cells*, 2016, **150**, 112-129.
46. P. Sinsermsuksakul, L. Z. Sun, S. W. Lee, H. H. Park, S. B. Kim, C. X. Yang and R. G. Gordon, *Adv. Energy Mater.*, 2014, **4**, 1400496.
47. B. Radisavljevic, A. Radenovic, J. Brivio, V. Giacometti and A. Kis, *Nat. Nanotechnol.*, 2011, **6**, 147-150.
48. S. Das, H. Y. Chen, A. V. Penumatcha and J. Appenzeller, *Nano Lett.*, 2013, **13**, 100-105.
49. C. Gong, L. Colombo, R. M. Wallace and K. Cho, *Nano Lett.*, 2014, **14**, 1714-1720.
50. H. Yuan, G. J. Cheng, L. You, H. T. Li, H. Zhu, W. Li, J. J. Kopanski, Y. S. Obeng, A. R. H. Walker, D. J. Gundlach, C. A. Richter, D. E. Ioannou and Q. L. Li, *ACS Appl. Mater. Interfaces*, 2015, **7**, 1180-1187.
51. in *CRC Handbook of Chemistry and Physics*, ed. J. R. Rumble, CRC Press/Taylor & Francis, Boca Raton, FL, (Internet Version) 98th edn., 2018, pp. 12-119.
52. D. E. Eastman, *Phys. Rev. B*, 1970, **2**, 1-2.
53. P. Villars, *Pearson's Handbook Desk Edition: Crystallographic Data for Intermetallic Phases*, ASM International, Materials Park, OH, 1997.
54. A. J. Biacchi, S. T. Le, B. G. Alberding, J. A. Hagmann, S. J. Pookpanratana, E. J. Heilweil, C. A. Richter and A. R. Hight Walker, *submitted*.
55. B. G. Alberding, A. J. Biacchi, A. R. H. Walker and E. J. Heilweil, *J. Phys. Chem. C*, 2016, **120**, 15395-15406.
56. X. L. Tang, H. W. Zhang, H. Su and Z. Y. Zhong, *Phys. E*, 2006, **31**, 103-106.
57. Z. Y. Zhang, K. Yao, Y. Liu, C. H. Jin, X. L. Liang, Q. Chen and L. M. Peng, *Adv. Funct. Mater.*, 2007, **17**, 2478-2489.
58. J. Osvald, *Phys. Status Solidi A*, 2015, **212**, 2754-2758.

59. A. J. Chiquito, C. A. Amorim, O. M. Berengue, L. S. Araujo, E. P. Bernardo and E. R. Leite, *J. Phys.: Condens. Matter*, 2012, **24**, 225303.
60. R. Nouchi, *J. Appl. Phys.*, 2014, **116**, 184505.
61. E. H. Rhoderick and R. H. Williams, *Metal-Semiconductor Contacts*, Clarendon Press, New York City, 2nd edn., 1988.
62. S. M. Sze and K. K. Ng, in *Physics of Semiconductor Devices*, J. Wiley & Sons, Hoboken, NJ, 3rd edn., 2007, ch. 3, pp. 134-196.
63. F. A. Padovani and R. Stratton, *Solid-State Electron.*, 1966, **9**, 695-707.
64. D. K. Schroder, *Semiconductor Material and Device Characterization*, J. Wiley & Sons, Hoboken, NJ, 3rd edn., 2006, ch. 3, pp. 127-184.
65. H. R. Chandrasekhar, R. G. Humphreys, U. Zwick and M. Cardona, *Phys. Rev. B*, 1977, **15**, 2177-2183.
66. L. M. Yu, A. Degiovanni, P. A. Thiry, J. Ghijsen, R. Caudano and P. Lambin, *Phys. Rev. B*, 1993, **47**, 16222-16228.
67. R. E. Banai, L. A. Burton, S. G. Choi, F. Hofherr, T. Sorgenfrei, A. Walsh, B. To, A. Croll and J. R. S. Brownson, *J. Appl. Phys.*, 2014, **116**, 013511.
68. J. Appenzeller, M. Radosavljevic, J. Knoch and P. Avouris, *Phys. Rev. Lett.*, 2004, **92**, 048301.
69. V. Stevanovic, K. Hartman, R. Jaramillo, S. Ramanathan, T. Buonassisi and P. Graf, *Appl. Phys. Lett.*, 2014, **104**, 211603.
70. W. Albers, H. J. Vink, C. Haas and J. D. Wasscher, *J. Appl. Phys.*, 1961, **32**, 2220-2225.
71. A. J. Biacchi, D. D. Vaughn and R. E. Schaak, *J. Am. Chem. Soc.*, 2013, **135**, 11634-11644.
72. S. Karadeniz, M. Sahin, N. Tugluoglu and H. Safak, *Semiconductor Science and Technology*, 2004, **19**, 1098-1103.
73. A. W. Dweydari and C. H. B. Mee, *Phys. Status Solidi A*, 1975, **27**, 223-230.
74. A. de Kergommeaux, J. Faure-Vincent, A. Pron, R. de Bettignies, B. Malaman and P. Reiss, *J. Am. Chem. Soc.*, 2012, **134**, 11659-11666.
75. J. R. Chen, P. M. Odenthal, A. G. Swartz, G. C. Floyd, H. Wen, K. Y. Luo and R. K. Kawakami, *Nano Lett.*, 2013, **13**, 3106-3110.
76. A. Dankert, L. Langouche, M. V. Kamalakar and S. P. Dash, *ACS Nano*, 2014, **8**, 476-482.
77. W. Park, Y. Kim, S. K. Lee, U. Jung, J. H. Yang, C. Cho, Y. J. Kim, S. K. Lim, I. S. Hwang, H. B. R. Lee and B. H. Lee, *IEEE Int. Electron Devices Meet.*, 2014, 5.5.1-5.1.4.
78. S. Lee, A. Tang, S. Aloni and H. S. P. Wong, *Nano Lett.*, 2016, **16**, 276-281.
79. H. H. Berger, *Solid-State Electron.*, 1972, **15**, 145-158.
80. H. Murrmann and D. Widmann, *IEEE Trans. Electron Devices*, 1969, **16**, 1022-1024.
81. C. W. Bale, E. Belisle, P. Chartrand, S. A. Decterov, G. Eriksson, A. E. Gheribi, K. Hack, I. H. Jung, Y. B. Kang, J. Melancon, A. D. Pelton, S. Petersen, C. Robelin, J. Sangster, P. Spencer and M. A. Van Ende, *CALPHAD: Comput. Coupling Phase Diagrams Thermochem.*, 2016, **54**, 35-53.
82. R. L. Gurunathan, J. Nasr, J. J. Cordell, R. A. Banai, M. Abraham, K. A. Cooley, M. Horn and S. E. Mohny, *J. Electron. Mater.*, 2016, **45**, 6300-6304.
83. G. S. Marlow and M. B. Das, *Solid-State Electron.*, 1982, **25**, 91-94.
84. S. E. Mohny, Y. Wang, M. A. Cabassi, K. K. Lew, S. Dey, J. M. Redwing and T. S. Mayer, *Solid-State Electron.*, 2005, **49**, 227-232.
85. H. Park, R. Beresford, R. Ha, H. J. Choi, H. Shin and J. Xu, *Nanotechnology*, 2012, **23**, 245201.
86. G. K. Reeves and H. B. Harrison, *IEEE Electron Device Lett.*, 1982, **3**, 111-113.
87. L. B. Hou, Q. J. Bu, S. Li, D. J. Wang and T. F. Xie, *RSC Adv.*, 2016, **6**, 99081-99087.
88. Y. P. Liao, K. Pan, Q. J. Pan, G. F. Wang, W. Zhou and H. G. Fu, *Nanoscale*, 2015, **7**, 1623-1626.

89. Y. B. Zhu, X. H. Zhang, J. L. Song, W. Wang, F. F. Yue and Q. Ma, *Appl. Catal., A*, 2015, **500**, 51-57.

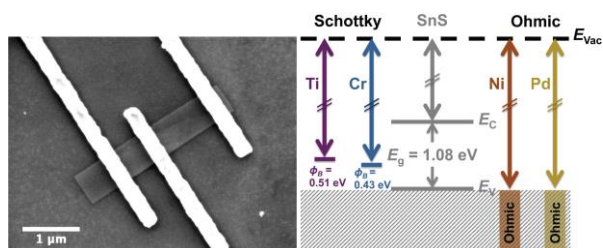
^a Department of Materials Science and Engineering, Carnegie Mellon University, Pittsburgh, PA 15213

^b Engineering Physics Division, National Institute of Standards and Technology (NIST), Gaithersburg, MD 20899

* Email: jhajzus@andrew.cmu.edu

†Electronic supplementary information (ESI) available.

Table of Contents Image



Four different metals were patterned onto individual, solution-synthesized SnS nanoribbons to determine Schottky barrier heights and specific contact resistances.